INSTITUTE OF PHYSICS PUBLISHING SMART MATERIALS AND STRUCTURES
Smart Mater. Struct. **10** (2001) 1145–1155 PII: S0964-1726(01)29657-8

Microrockets for Smart Dust

Dana Teasdale, Veljko Milanovic, Paul Chang and Kristofer S J Pister

Berkeley Sensor and Actuator Center (BSAC), University of California, Berkeley, 497 Cory Hall #1770, Berkeley, CA 94720-1770, USA

E-mail: veljko@eecs.berkeley.edu

Received 10 April 2000, in final form 29 August 2000
Published 26 November 2001
Online at stacks.iop.org/SMS/10/1145

Abstract

This paper details the design and fabrication of millimeter-scale solid propellant rockets for one-time deployment of wireless sensor platforms, known as Smart Dust. Each microrocket assembly is an integrated system, incorporating a combustion chamber, composite propellant grain, nozzle, igniter, and thermoelectric power converter. Solid propellant is advantageous for a millimeter-scale single-use device because of its simple implementation, unlike liquid propellants, which require a more elaborate system of pumps and valves. Therefore the total system volume and complexity are minimized.

One type of combustion chamber was fabricated in silicon; however, thermal losses to the silicon sidewalls during combustion through a 1.5 mm^2 cross section of fuel were too high to reliably maintain a burn. Successful combustion was demonstrated in cylindrical alumina ceramic combustion chambers with thermal conductivities five times lower than silicon and cross sections of 1–8 mm^2. Thrusts of 10–15 mN were measured for ceramic rockets weighing under 1 g, with specific impulses up to 15 s.

Silicon nozzles integrated with polysilicon microheaters and thermopiles for thermal power conversion were microfabricated in a single process. Fuel ignition by polysilicon microheaters suspended on a low-stress nitride (LSN) membrane was demonstrated. Microheaters require less than 0.5 W of power to ignite a propellant composed primarily of hydroxyl-terminated polybutadiene (HTPB) with ammonium perchlorate (AP) oxidizer. They are suspended for thermal isolation through bulk post-processing by a backside deep reactive ion etch (DRIE). The etched hole beneath the igniter area also serves as a nozzle through which high-velocity combustion gases exit the rocket. Thermopiles, which generate voltages proportional to hot and cold junction temperature differentials, have been fabricated in the same process as igniters, and span backside DRIE thermal isolation cavities. Ten-junction thermopiles produced a maximum power of 20 μW. With potential temperature differences of hundreds of degrees and a total of 120 thermocouple junctions fabricated on the silicon nozzle chip, hundreds of milliwatts of power could feasibly be produced during the microrocket's flight and used to augment the Smart Dust power supply.

1. Introduction

From its inception, space exploration has been costly and hazardous due to the high cost of large, complex spacecraft and sometimes the endangerment of human lives. Trends in space-related industries are toward the miniaturization of spacecraft and space systems [1]. Decreasing the size of space systems requires the miniaturization of environmental monitoring components and propulsion systems.

Advances in the fields of digital circuitry, wireless communications and microelectromechanical systems (MEMS) converge in the development of tiny, low-power, low-cost, autonomous sensor nodes known as Smart Dust, an ongoing research project at the Berkeley Sensor and Actuator Center [2].

Each Smart Dust mote is designed with its own suite of MEMS sensors, wireless communications, computing hardware, and a power supply, all within a few cubic millimeters (figure 1). Advances in line-of-sight optical communications using corner cube reflectors (CCR) [3] as passive transmitters and large dc deflection 2-DOF micromirrors for beam steering have been reported [4]. Additionally, preliminary platforms designed to test incoming optical signal decoding, generate simulated sensor data with a pseudorandom number generator, and drive a CCR have been designed and fabricated in a 0.25 μm CMOS process [5]. One important application for Smart Dust is monitoring environments in which data collection through wired networks or by humans may be difficult, such as outer space.

A micropropulsion system capable of flight with milligram payloads could be used to distribute Smart Dust motes from a base station. Multiple hop communication between Smart Dust motes is feasible when motes are within approximately 1 km of each other. Therefore, a network of motes can be generated, allowing data from remote sites, or potentially around an entire planet, to be collected at a central station, such as a satellite. Smart Dust deployment by microrockets would expand the area and sensor density through which monitoring could be performed.

Miniaturizing a rocket system presents unique challenges:

- Propellant—a high energy density propellant that combusts through small cross sections and has chemical reaction rates fast enough that combustion is completed during the propellant's residence time in the combustion chamber is required.
- Assembly and fabrication—combustion chambers must provide thermal insulation to burning propellant and sustain high internal pressures. The use of microfabrication techniques is desirable due to batch fabrication, low cost, and integration with several micromachined components.
- Ignition—adequate energy must be supplied by a microfabricated structure to ignite the propellant.

Previous work towards the development of low-thrust micropropulsion systems with nanosatellite and microsatellite station-keeping and maneuvering applications has been carried out. Janson *et al* [6] discuss microfabricated cold gas thrusters, digital thruster arrays, resistojets, and field ion engines. Thrust-producing devices have been fabricated through various micromachining processes with measured thrusts up to 1 mN for cold gas thrusters, and impulses in the 0.09 mN s range for the digital thrusters. The digital thruster arrays operate explosively, by breaking a membrane directly following ignition. In these systems, fuel often exits the thruster nozzle uncombusted. Other solid propellant microthrusters were developed by Rossi *et al* [7], with measured thrusts of up to 9.8 mN. While effectively producing the thrust levels required for some microsatellite and nanosatellite positioning applications, none of these systems have been designed specifically for flight.

This paper describes the design and fabrication of a microrocket designed for one-time deployment of Smart Dust motes through rocket flight. The microrocket system presented integrates the rocket propellant, a ceramic combustion chamber, silicon micromachined nozzle, polysilicon igniter, and thermal power converters. Micromachining techniques enable the fabrication of the polysilicon igniter and thermopiles for thermal power conversion to be completed in the same process, all on a silicon substrate backside etched to become the rocket nozzle.

2. Propellant

Despite demonstrated rocket propulsion by methods including nuclear thermal rockets, ion propulsion, and Hall effect thrusters, chemical rocket engines remain the most commonly used [8]. Chemical reactants are second only to nuclear fuels in terms of energy density [9]. Chemical propellants have also been widely researched and used reliably in applications ranging from booster rockets for the space shuttle to numerous hobby rockets.

The characteristics of different types of chemical rocket propellants were investigated to choose the most appropriate fuel for a microrocket. The two most common types of chemical propellants are solid and liquid (figure 2). In solid propellants, the fuel and oxidizer are both present in solid form, can be stored at room temperature, and are easy to use without special operating and handling equipment. Liquid propellants are composed of liquid fuels and oxidizers that are stored separately and mixed at the time of combustion. They require systems for storage and usage, including pumps, valves, and sometimes cryogenic storage tanks. For some applications, however, the complexity of handling liquid propellants is warranted because they often have higher specific impulses than solids, and combustion can be readily throttled or stopped altogether. Specific impulse describes the total force integrated over burning time per unit weight of the propellant, and can be estimated by Ft/mg, where F is thrust (N), t is time (s), m is propellant mass (kg), and g is the gravitational constant (m s^{-2}).

Special consideration in the development of a microrocket must be given to fuel energy density, specific impulse, flammability limits, fabrication capabilities, and system complexity. To achieve the smallest overall structure while preserving design simplicity and relatively high specific impulse, a solid, composite fuel with ammonium perchlorate oxidizer (AP) was chosen. The composite fuel used contains 74% AP, with hydroxyl-terminated polybutadiene (HTPB) fuel binder, along with the other ingredients listed in table 1 [10]. Solid propellants with AP oxidizer generally have energy densities of approximately 5 kJ g^{-1} and specific impulses of 220–260 s (for 1000 psi chamber pressure), of the order of many liquid hydrocarbon propellants.

Variations in the AP particle size in the propellant mixture were observed to have an impact on the propellant's capacity to burn through small cross-sectional areas. The propellant mixture, containing AP particles which were ground smaller than their original 200 μm diameter, was found to ignite and sustain combustion through small cross sections more readily than the mixture containing only 200 μm particles. Kishore and Gayathri [11] show that composite propellant combustion relies on the decomposition of oxidizer and fuel into gases that mix and combust in the presence of heat (figure 3). If the oxidizer particles are large and spaced far apart, the gasified oxidizer and fuel may not mix adequately in a small chamber to maintain the exothermic combustion process.

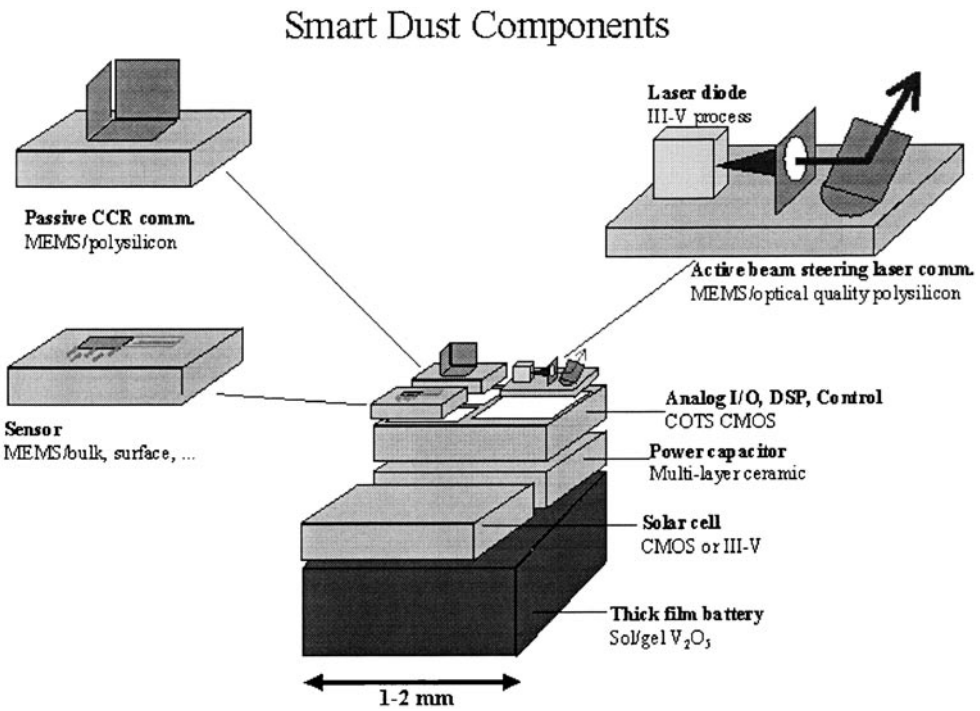

Figure 1. Smart Dust components.

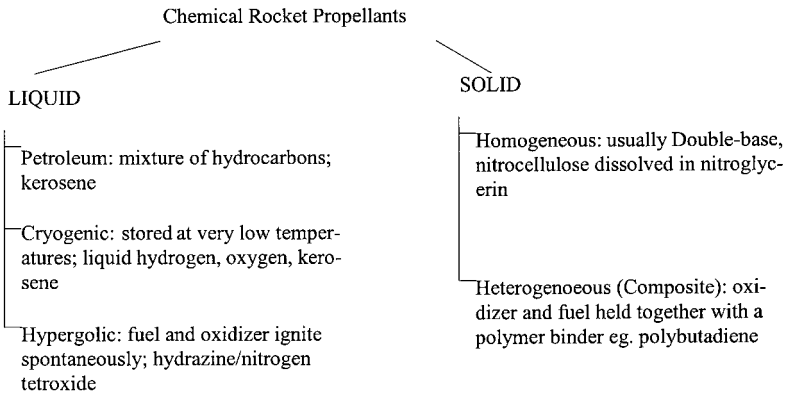

Figure 2. Schematic diagram of types of chemical rocket propellants.

Table 1. Propellant ingredients [10].

Ingredient	% by mass	Function
Ammonium perchlorate, 200 μm	74	Oxidizer
R45-M resin (HTPB)	14	Binder/fuel
2-ethylhexyl acrylate (EHA)	6.5	Plasticizer
Isophorone diisocyanate (IPDI)	3.5	Curing agent
Fe_2O_3	1.25	Combustion catalyst
HX-878 (Tepanol)	0.75	Bonding agent

Adding aluminum (Al) particles to composite propellants is often done to increase the burn rate, flame temperature, or energy density of the fuel. Al was added to the HTPB/AP composite fuel, and ignited by a thin wire filament inside a $3 \times 4 \times 1.5$ mm ceramic combustion chamber. The added Al did result in an increase in burn rate; however, Al particles were visibly combusting after exiting the chamber, and were found to clog sub-millimeter nozzles. This agrees with Sigman *et al* [12] that, during combustion, Al particles tend to agglomerate at the burning surface and exit the combustion chamber without fully burning. A comparison between combustion flames for HTPB/AP and HTPB/AP/Al in $3 \times 4 \times 1.5$ mm ceramic combustion chambers is shown in figures 4(*a*) and (*b*). This result is an indication of how scaling can affect rocket performance; the residence time of combustion species in the combustion chamber must be longer than chemical combustion reaction rates. HTBP/AP fuel mixture without Al was used for all subsequent testing.

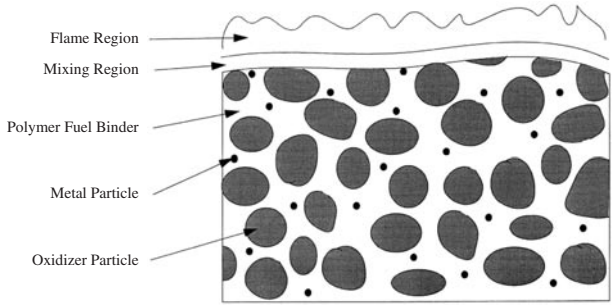

Figure 3. Diagram of heterogeneous (composite) solid propellant oxidizer particles suspended in the fuel binder. Mixing of gaseous fuel and oxidizer occurs directly above the propellant surface and below the flame.

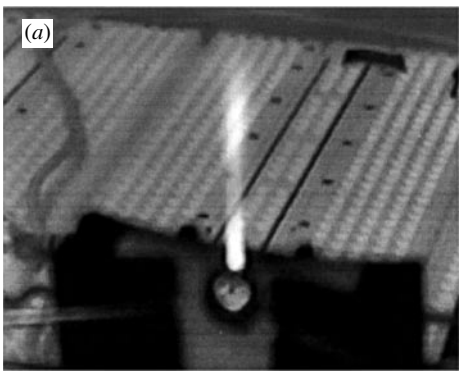

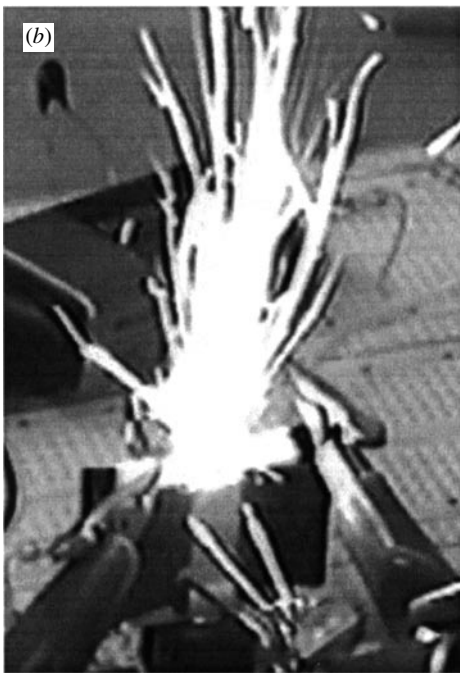

Figure 4. (*a*) HTPB/ATP combustion in a 3 × 4 × 1.5 mm ceramic combustion chamber. (*b*) HTPB/AP/Al combustion in the same chamber. Al particles can be seen combusting outside the rocket.

3. Rocket assembly and fabrication

The rocket assembly has two basic components: a combustion chamber and a nozzle. The combustion chamber houses the solid propellant, while the nozzle is a constriction at the combustion chamber exit that allows hot combustion gases to accelerate as they exit the rocket, thereby increasing thrust. Igniters and power-converting thermopiles are fabricated on the same silicon substrate that the nozzle is etched into, and will be discussed in more detail in subsequent sections.

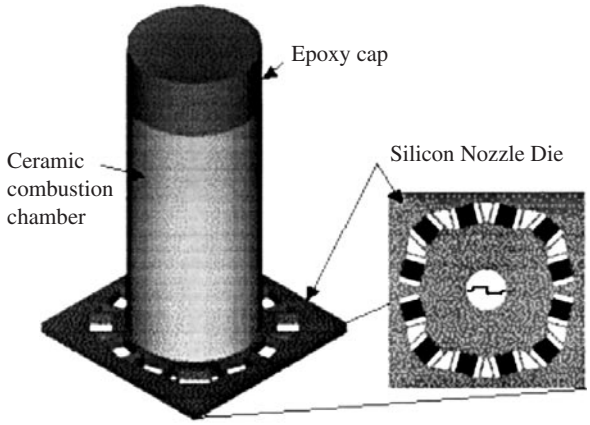

Figure 5. Rocket assembly and nozzle layout view. The igniter spans the nozzle in the center and thermopiles are placed around the outer edge of the chip.

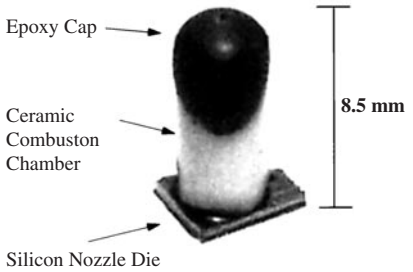

Figure 6. Assembled microrocket. Ceramic combustion chamber epoxied to the silicon nozzle die.

Each rocket system is assembled by packing uncured propellant into the ceramic combustion chamber, allowing the propellant to cure, and bonding the propellant-filled combustion chamber and the nozzle die together with high-temperature epoxy. The open end of the combustion chamber is also sealed with epoxy. Figure 5 shows a design rendering of the rocket assembly, giving details of the nozzle, and figure 6 shows the assembled microrocket.

3.1. Combustion chamber

In preliminary tests, 2D combustion chambers and nozzles were fabricated in copper, aluminum, brass, carbon steel, and stainless steel plates by wire electrical discharge machining (EDM), and in ceramic by conventional machining. Chambers with similar geometries, as shown in figure 7, were fabricated in silicon using deep reactive ion etch (DRIE). In this process, wafers of silicon combustion chambers were fabricated with a single photolithography step followed by DRIE through the wafer. The combustion chambers were filled with HTPB/AP composite fuel and sealed by epoxying glass plates to the chambers. Ignition was achieved by heating a thin wire filament in contact with the fuel at the nozzle opening. Testing showed that, at room temperature, combustion was difficult

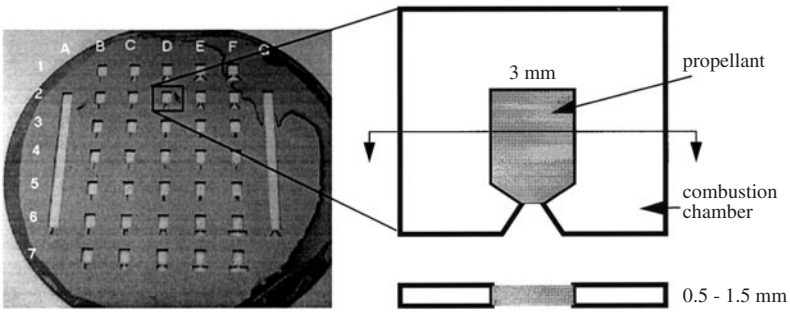

Figure 7. Silicon wafer with DRIE combustion chambers and nozzles and details of the chamber design.

to sustain through the entire length of the 2D combustion chamber, with the only repeatable sustained burn occurring in the ceramic combustion chamber. Therefore, a combustion chamber material with low thermal conductivity is necessary, since heat loss through the chamber walls removed enough energy from the burning fuel to quench combustion in the silicon and metal chambers. Additionally, the 1.5 mm glass covers to the chambers were found to break during combustion due to the high pressures generated in the combustion chamber, indicating the need for stronger chamber walls.

An alumina ceramic cylindrical combustion chamber design addresses the needs of thermal insulation and strength. Alumina ceramic has a thermal conductivity of 30 W m K^{-1}, five times lower than the thermal conductivity of silicon. Additionally, the cylindrical shape reduces the surface area by 13% compared to a 1.5 mm thick rectangular chamber having the same length and volume. This also serves to reduce the overall volume occupied by the chamber since less wall surface is required, thus reducing the mass of the rocket. The cylindrical chamber also has a structural advantage over the flat, rectangular chamber since it is able to resist bending, which the walls of the rectangular chamber are prone to.

Overall, alumina ceramic cylindrical combustion chambers offer low thermal conductivity, decreased surface area, decreased total volume, and increased structural integrity when compared to 2D silicon and metal chambers. The main disadvantage of alumina ceramic cylinders is that they are not microfabricated, and must be machined separately. A more exhaustive investigation of materials and chamber geometries is required to minimize combustion chamber mass, volume, and thermal conductivity while maintaining strength.

3.2. Nozzle

The nozzle portion of the rocket is fabricated using silicon micromachining techniques, which allow the integration of an igniter and thermopile for power conversion into each rocket nozzle. Igniters and thermopiles are surface micromachined out of polysilicon and aluminum conductive layers, with low stress nitride (LSN) insulating layers, as shown in steps 1–5 of figure 8. In step 6, surface micromachining is followed by a backside DRIE through the 300 μm thick silicon wafer. The backside etch creates the nozzle opening and thermal isolation cavities. When these cavities are created, the igniter and thermopiles are suspended on LSN membranes.

The patented Bosch process, as described in [13], is used in the backside DRIE to form the nozzle and thermal isolation

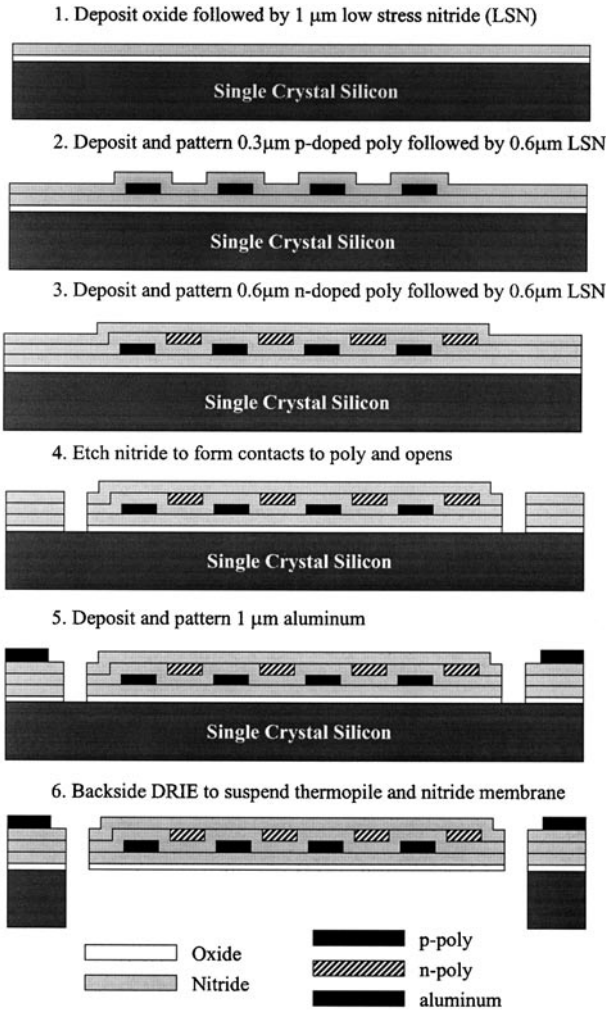

Figure 8. Process flow showing thermopile fabrication. Igniters and nozzles are made in the same process.

holes. This process etches deep, high aspect ratio trenches in silicon. As a result, nozzles with negligible expansion angles are formed. Fabrication of micronozzles by means of an anisotropic KOH etch through a wafer was reported by Janson and Helvajian [6]. KOH etches silicon selectively along the ⟨100⟩ planes, while almost stopping on the ⟨111⟩ planes, resulting in a 35° nozzle expansion, which refers to the angle between the nozzle edge and the centerline. In general, a nozzle is considered optimal when the pressure of the gas

as it exits the nozzle is the same as the ambient pressure. Typical optimized macroscale rocket nozzles are designed with 15°–20° expansions; however, considering the larger relative boundary effects for micronozzles, these may not be the optimal angles for microscale nozzles. In comparison, the DRIE nozzles are underexpanded while the KOH-etched nozzles are overexpanded. In either case, nozzle efficiency is not optimized, but the underexpanded case is generally preferable to the overexpanded case since the drag and non-axial component of the gas velocity are smaller. Early gas expansion micronozzles fabricated in PMMA using only X–Y laser micropositioning (all angles are 90°) were reported by Janson and Helavijian [14] as having I_{sp} values up to 83% of the ideal I_{sp} values, suggesting that significant thrust can be generated when using crude nozzle geometries. Bayt *et al* [15] have fabricated micronozzles for cold gas expansion using DRIE in the plane of the wafer such that nozzle geometries can be more easily controlled, with reported mass flow efficiencies of 87–98%.

4. Ignition

Ignition occurs when energy is introduced to the propellent through exposure to a hot surface, radiant energy source, hot inert gas, pilot flame, explosive charge, or electrical spark. Leading up to ignition, external heating of the propellant creates a temperature rise sufficient to initiate chemical reactions at the propellant surface. These chemical reactions are exothermic, and they further increase the temperature and chamber pressure until ignition occurs and steady-state combustion begins. This process occurs at near 600 °C for HTPB/AT propellants.

Factors influencing ignition include igniter temperature, duration that the propellant is exposed to the igniter, and area of fuel surface exposed to the hot igniter surface. Strong, or high power, sources that reach temperatures near the propellant flame temperature tend to ignite the propellant quickly, while weak sources require a longer exposure time [16].

An array of polysilicon heaters was fabricated using the process described in figure 8. The array consisted of straight and meandering heater designs with polysilicon widths ranging from 8 to 80 μm, lengths varying from 450 to 1050 μm, and an n-doped polysilicon thickness of 0.3 μm with a sheet resistance of 25 $\Omega/\square$. Heaters were tested for their ability to ignite the HTPB/AP propellant by placing a small slab of propellant directly on top of the suspended heaters. Ignition was achieved by three meandering heater designs, and no straight designs. The lengths, widths and resistances of successful igniters are given in table 2. Figure 9 is a scanning electron micrograph of a suspended polysilicon heater, with an inset of its measured heating profile. Thermal isolation through suspending the heater on a membrane localizes high temperature regions on the heater, with little heat dissipation to the surroundings areas.

In order to increase the reliability and area over which heat is generated by the polysilicon igniters, three polysilicon heaters of heater 1 type (from table 2) were connected in parallel and suspended over the 1 mm diameter nozzle opening in an LSN membrane. This design was robust in the sense that ignition was still achievable even when there was damage to one or two of the suspended heaters, and in some trials, heaters were still functional after fuel burned directly on top of them.

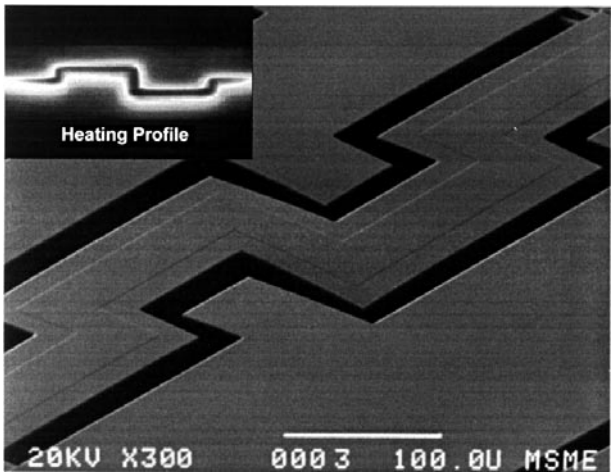

Figure 9. Polysilicon igniter suspended on an LSN membrane. Inset: measured heating profile at 8 V, 2.6 mA. Maximum temperature = 182 °C.

Table 2. Polysilicon igniter characteristics.

	Length (μm)	Width (μm)	Resistance (kΩ)
Heater 1	1050	16	2.65
Heater 2	1050	8	5.95
Heater 3	850	40	0.80

Table 3. Properties of p-poly and n-poly igniters.

Property	P-poly	N-poly
Thickness (μm)	0.6	0.3
Resistance (kΩ)	1.1	0.6
V_{ignition} (V)	25	15
P_{ignition} (W)	0.3	0.2

Both n- and p-poly igniters were fabricated using the three parallel igniter design, with a p-poly thickness of 0.6 μm and an n-poly thickness of 0.3 μm. Sheet resistances of p-poly and n-poly were 30 $\Omega/\square$ and 15 $\Omega/\square$, respectively. Functionality was once again demonstrated by placing fuel directly on the suspended heaters and increasing the dc voltage to the point of ignition. Ignition occurred with input voltages of 25 V for p-doped poly and 15 V for n-doped poly. Although current was not measured directly, power supply current outputs of 10–15 mA were observed at the time of ignition for both types of igniters. The total power supplied during ignition is then estimated to be 0.3 W for p-poly and 0.2 W for n-poly. Properties for p- and n-doped igniters of the same design are summarized in table 3.

Igniters were tested with and without fuel loading to determine the time constant associated with resistor heating. The time constant reflects the time required by the heater to increase in temperature once a voltage is applied. To determine the igniter's time constant, a step voltage was applied to the heater in series with a known resistor. By measuring the voltages across the heater and across the series resistor, the current was calculated and used to determine heater resistance. Resistance values were used to determine heater temperature

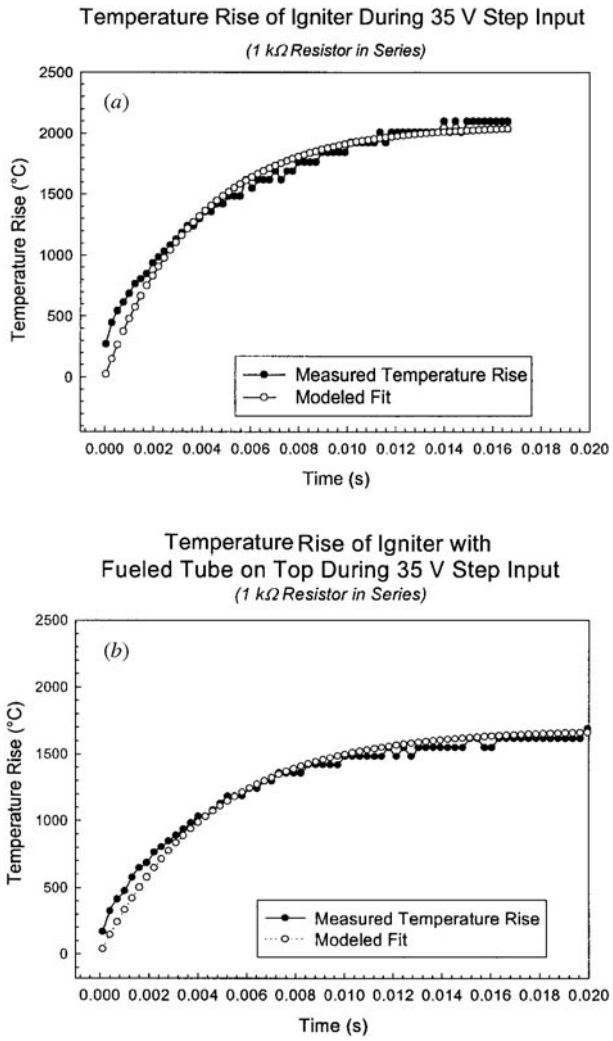

Figure 10. Temperature rise of a p-poly igniter (*a*) without fuel loading ($\tau = 4.6$ m s), and (*b*) with a ceramic tube filled with fuel on top of the heater ($\tau = 3.8$ m s).

assuming a thermal coefficient of resistance of 1×10^{-3} K^{-1} for polysilicon. The thermal time constant, τ, a function of the thermal resistance and thermal capacitance, was then determined by correlating the data with

$$\Delta T = a\left(1 - \mathrm{e}^{\frac{-t}{\tau}}\right)$$

where T is the temperature (K), a is a constant reflecting the input power and thermal resistance, and t is time (s). Figure 10 shows the plots of igniter temperature rise versus time during 35 V step input for a p-poly igniter with no fuel load and an igniter with a propellant-filled ceramic cylinder placed on it. The time constants are 4.6 and 3.8 m s, respectively.

Despite the millisecond time constant of the igniter, ignition does not occur quite so quickly. The igniter heat only begins the reactions that develop into all-out combustion. The total ignition time delay was measured using the thermopiles on the outer edges of the nozzle chip to determine the time of ignition, occurring sometime after a voltage is applied across the heater. The ignition time delay, once maximum heater power is reached, was measured to be anywhere from 0.02–1.5 s after the heater voltage is applied. Measured igniter power inputs of 0.2–0.3 W result in a total energy input to the system during ignition of between 4–300 mJ. It is unclear why such a wide range of ignition time delays were observed. Possible explanations include varied doping and thickness of the polysilicon heaters due to process variations, nonuniformities in the propellant grain, or differing contact areas between the propellant and the igniter.

5. Thrust measurement

A thrust measurement device was designed and built to test microrocket thrust. The device operates by attaching the rocket to a rigid pendulum. A force sensor is placed so that it is touching the pendulum arm, and the output signal from the force sensor is monitored when the rocket is ignited.

Thrust measurements were performed on rockets with cylindrical ceramic combustion chambers and nozzles at atmospheric pressure and room temperature. Combustion chambers had diameters of 0.319 cm and lengths of either 1.27 cm or 2.54 cm. Ceramic nozzles had no divergence, a throat diameter of 0.157 cm, and lengths of either 0.635 cm or 1.27 cm. A commercial wire filament igniter was used by inserting it into small holes in the combustion chamber near the nozzle. Despite the non-optimal nozzle and observations that some exhaust exited the igniter holes, initial thrust peaks of up to 15 mN were measured, followed by sustained 2 mN thrust for the remainder of the burn time. Burn rates were typically 1.4 mm s^{-1}.

Testing of integrated microrockets with cylindrical ceramic chambers and silicon nozzle chips with polysilicon igniters yielded similar results to ceramic-only microrocket thrust testing. Again, an initial peak was observed, followed by a steady burn, as shown in figure 11. Although the thrusts generated are not high enough for most flight applications on the Earth's surface, the low thrust may be well suited to applications for space systems. Specifically, for the thrust curve in figure 23, enough thrust is generated to accelerate the rocket's 0.75 g mass at 2.67 m s^{-2} for 7 s. Without the effects of gravity or drag, a velocity of approximately 20 m s^{-1} and distance of 65 m would be reached by the end of the burn.

6. Power conversion

The total energy available in the microrocket system is the propellant energy plus the input ignition energy. Burning 0.1 g of a 5 kJ g^{-1} fuel yields 500 J, and the igniter energy input provides an additional 3–400 mJ. Only a small fraction of this energy is converted into kinetic energy to move the rocket, while much of it is dissipated as heat. Therefore, a thermal gradient of potentially hundreds of degrees can exit between the combustion flame front and the outer edges of the rocket. Thermocouples are often used as thermal sensors because they convert temperature differences into proportional voltages. The thermoelectric effects that govern this type of thermal conversion make thermopiles, or multiple junction thermocouples, useful energy converters capable of converting thermal energy into electrical energy.

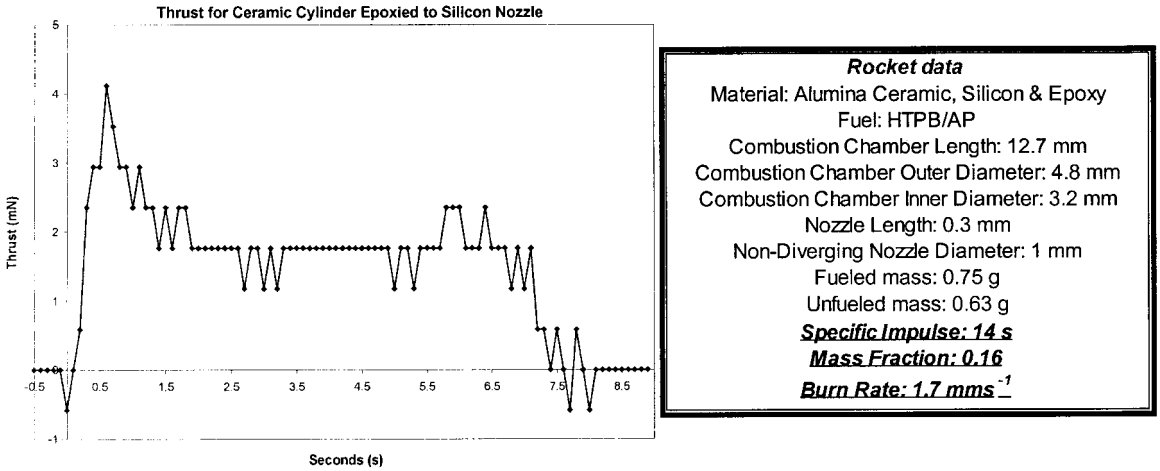

Figure 11. Thrust curve for integrated microrocket assembly: ceramic combustion chamber epoxied to silicon nozzle.

6.1. The Seebeck effect

The thermoelectric effect discovered by Seebeck in 1826 addresses the material property of electrical conductors and semiconductors to convert a temperature difference into an electrical potential, or Seebeck voltage (V_s). When two different conductors are in contact in a hot region (T_h) and the unconnected ends remain at a lower temperature (T_l), the Seebeck voltage generated is related to the temperature difference by [17]

$$V_S = \int_{Th}^{Tl} \alpha a(T)\,\mathrm{d}T + \int_{Th}^{Tl} \alpha b(T)\,\mathrm{d}T \cong (\alpha_a - \alpha_b)\Delta T$$

where α_a and α_b are the Seebeck coefficients for conductors a and b. The Seebeck coefficient of a conductor is usually given in units of μV K^{-1} or mV K^{-1}. Such a device, with two legs of different conducting materials, is called a thermocouple. N thermocouples connected electrically in series form a thermopile, and can produce up to N times the voltage output of a single thermocouple. Although larger voltages can be reached by thermocouple materials with high relative Seebeck coefficients (α_a–α_b) than by those with lower relative Seebeck coefficients, often high relative Seebeck coefficients correspond to high resistivity and high thermal conductivities, which decreases overall thermal conversion efficiency. Therefore, materials with high Seebeck coefficients, low electrical resistivity, and low thermal conductivity make the most efficient thermal power converters.

Advances in mechanical microsensor fabrication in MEMS and complementary metal oxide semiconductor (CMOS) technologies [17, 18] make the integration of thermal converters in a microrocket assembly possible. Seebeck coefficients have been characterized for standard CMOS conductors [18–21]. The highest relative Seebeck coefficient for the ORBIT 1.2 μm process is 785 μV K^{-1} for n-poly/p$^+$-active layer thermocouples [21].

6.2. Thermal simulation

Simulations were performed to determine the steady-state temperature profile of the silicon nozzle die that could be expected during rocket combustion. Silicon nozzle dies of varying sizes and volumes of thermal isolation holes were simulated to determine the effectiveness of the thermal isolation holes etched beneath the thermopile structures. The plot in figure 12 shows simulated temperature distributions for various thermal isolation hole patterns along the silicon surface, starting from the nozzle and progressing radially outward. This simulation assumes a constant 1000 K at the nozzle opening and 300 K ambient temperature under convective air flow conditions. It is clear that increasing the volume of holes around the 'thermal isolation ring', the donut-shaped area separating hot and cold thermopile junctions, results in larger temperature differentials from one side of the ring to the other. The size of the isolation holes does not seem to be much of a factor, given that the same total hole volume is removed in the additional large and small hole cases. According to the simulation, the steady-state temperature difference between the hot side of the thermopile and the cold side of the thermopile is approximately 125 K.

6.3. Testing

Thermocouple material combinations of n-poly, p-poly and aluminum were fabricated by the process described in figure 8. A fabricated n-poly/aluminum thermopile is shown in the micrograph in figure 13. Thermopiles made up of ten thermocouple junctions were fabricated and tested on chips similar to the nozzle die described in section 3.2. The test die did not have a nozzle hole such that the polysilicon heater was heating the substrate directly. p-poly/metal, n-poly/metal and n-poly/p-poly thermopiles were tested. Some of the thermopiles fabricated had their cold end positioned so that it was completely suspended over the cavity, while the rest had both hot and cold junctions located on the silicon with only the legs suspended over thermal isolation holes. Figures 14(a) and (b) show the voltage and power thermopile output plotted versus input heater power, where 200 mW of heater power corresponds roughly to a 70 K heater temperature rise. Thermopiles achieved steady-state output values within 1 s of heater turn-on, and required approximately 1.6 s to return to a nominal output value.

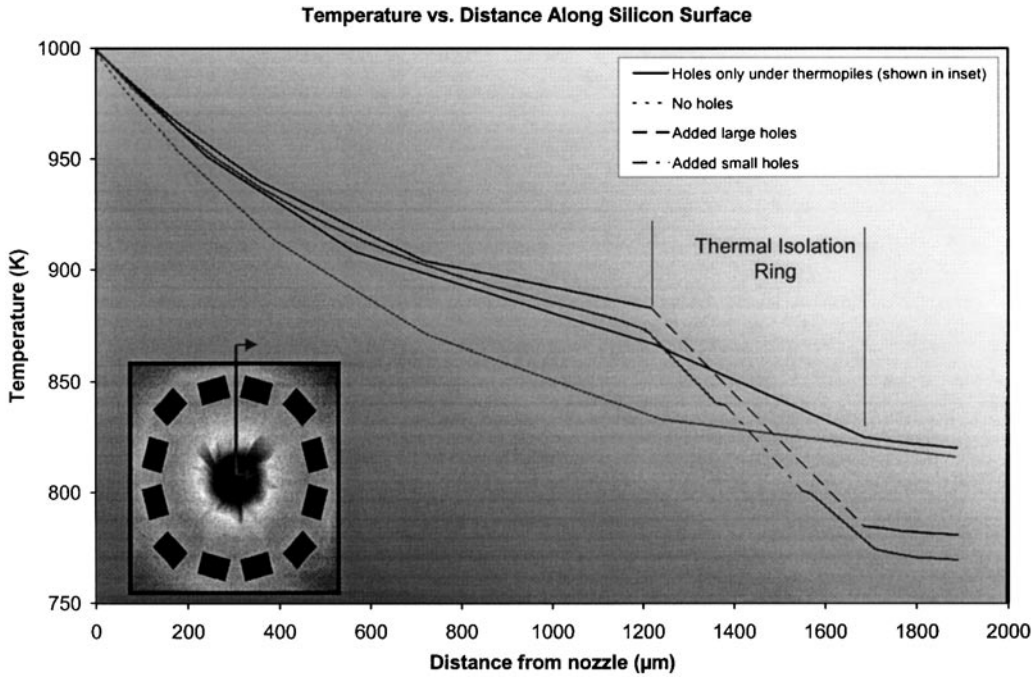

Figure 12. Plot of temperature versus distance along silicon surface. Various hole configurations in the thermal isolation ring are compared.

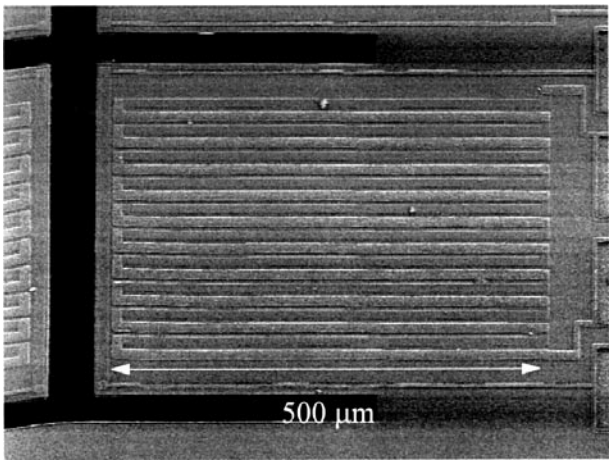

Figure 13. A 10-junction n-poly/aluminum thermopile suspended on an LSN membrane.

Correlating the 70 K heater temperature increase linearly with the 700 K simulated temperature differential from nozzle to chip edge, a 12.5 K temperature differential between the hot and cold side of the thermopile can be assumed. This corresponds to a Seebeck coefficient of 320 μV K^{-1} for p-poly/n-poly 10-junction thermopiles (32 μV K^{-1} per thermocouple), about 4% of the maximum reported values. Assuming a more optimal Seebeck coefficient of 785 μV K^{-1} for a p-poly/n-poly thermocouple junction, a 10-junction thermopile resistance of 50 kΩ, and that each chip has 12 such thermopiles, nearly 12 V and 60 μW could potentially be generated on a nozzle chip with a 125 K temperature differential. For a 7 s burn, this amounts to 9×10^{-7} of the total energy of the rocket system. However, with HTPB/AP flame temperatures capable of reaching over 3000 K, the simulated steady-state 125 K temperature differential can be considered conservative.

Thermopile voltages were monitored during combustion occurring on the nozzle die (with ignition performed by the polysilicon igniter). Sustained voltages of over 1.2 V per p-poly/n-poly 10-junction thermopile were observed during combustion. By placing a resistor of known resistance in series with the thermopile, power outputs of the 10-junction thermopile were measured with maximum values of 20 μW. This value is higher than the most optimistic predictions, probably because the temperature differential generated across the thermopiles is much larger than expected. For an array of twelve 10-junction thermopiles, hundreds of microwatts could be generated, which would certainly be adequate to drive low-power CMOS circuitry.

One difficulty encountered in drawing power from thermopiles is that, as a thermopile's voltage output increases, its resistance does as well, making it difficult to optimize power output for the entire burn time. Further experimentation is needed to determine the optimal load on a thermopile during operation.

In the rocket design presented, the nozzle die is considered fully populated with thermopiles when twelve 10-junction thermopiles are on the die. Increasing the number of thermocouple junctions placed around the rocket by making thinner legs, packing thermopiles more densely or using multiple tiers of thermopile rings is possible. This could potentially lead to much higher power output at the expense of more die surface dedicated to thermopiles.

A drawback to thermoelectrically generated power is that thermopiles will generate power only during propellant combustion since thermopiles rely on a thermal gradient. Current Smart Dust architecture provides for storage of electrical energy generated from solar radiation in an integrated capacitor. The same system would be utilized to store the excess generated energy from the thermopile system.

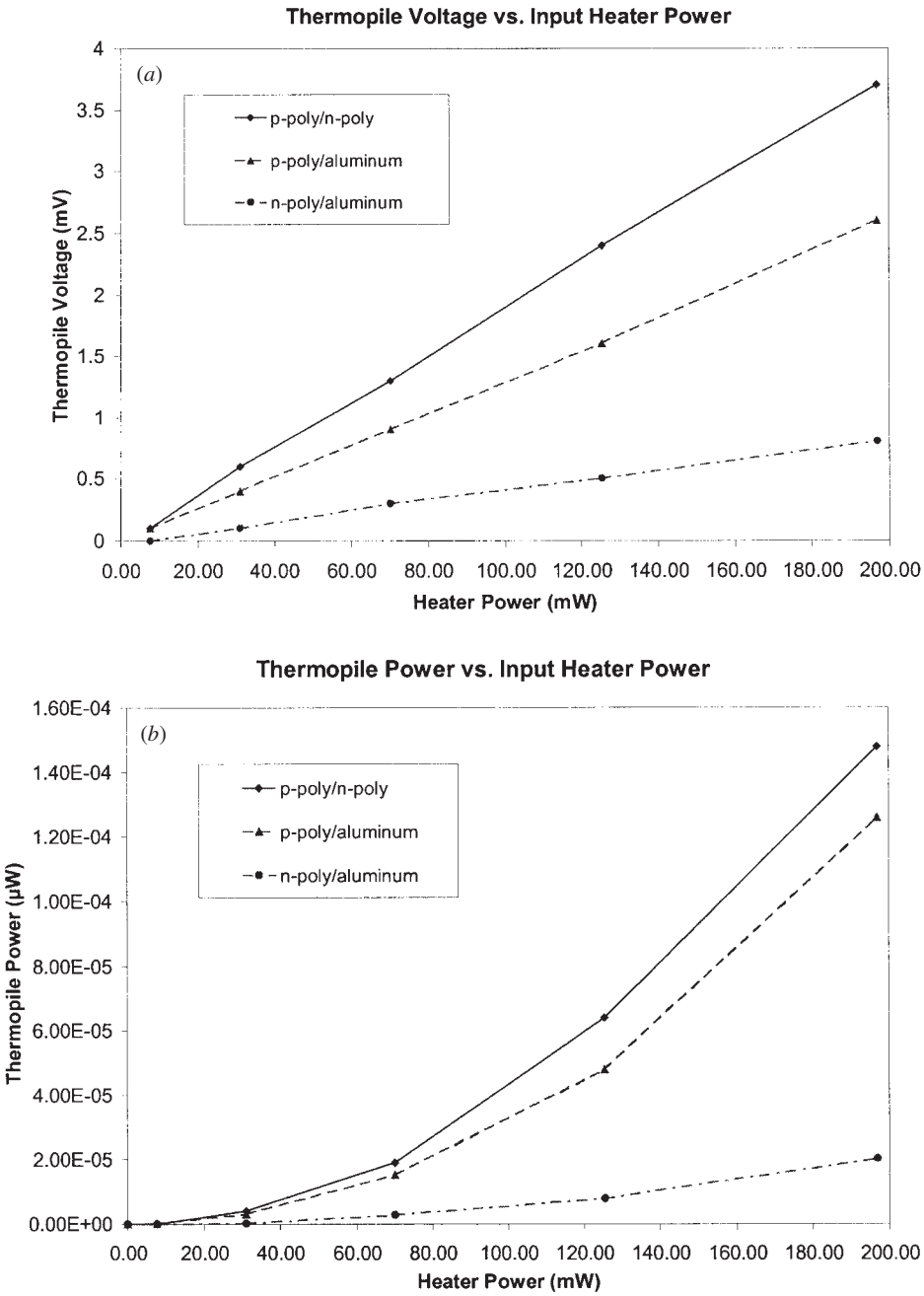

Figure 14. Plots of thermopile (*a*) voltage and (*b*) power versus heater power. N-poly/p-poly thermopiles generate the highest voltage and power.

7. Conclusions

Design and fabrication of millimeter-scale rockets have been presented. Microrockets with a mass less than 1 g are capable of producing thrust in the tens of mN for nearly half of a second. For 10 mN generated over 0.5 s, a velocity of 5 m s^{-1} can be reached by a 1 g microrocket in space carrying a Smart Dust payload. A microfabrication process for a microrocket nozzle integrated with polysilicon igniters and thermal power converters with backside-etched thermal isolation cavities has been completed. Ignition of HTPB/AP propellant by polysilicon resistive heaters has been demonstrated. Thermopiles were fabricated in the same process; n-poly/p-poly thermopiles generated the highest voltage and output power. Based on thermopile performance, hundreds of microwatts could potentially be generated by a rocket in flight for several seconds.

References

[1] 1998 4.0 Strategic Technology Areas, NASA Technology Plan, http://technologyplan.nasa.gov

[2] Kahn J M, Katz R H and Pister K S J 1999 Mobile networking for Smart Dust *ACM/IEEE Int. Conf. on Mobile Computing and Networking (MobiCom 99) (Seattle, WA Aug. 1999)*

[3] Hsu V, Kahn J M and Pister K S J 1998 Wireless communications for Smart Dust *Electronics Research Laboratory Technical Memorandum Number* M98/2

[4] Last M and Pister K 2DOF Actuated micromirror designed for large dc deflection *MOEMS 99*

[5] Atwood B, Warneke B and Pister K 2000 Preliminary circuits for Smart Dust *2000 Southwest Symp. on Mixed-Signal Design (Feb. 2000)*

[6] Janson S W, Helvajian H, Hansen and Lodmell W Lt. J 1999 Microthrusers for nanosatellites *Proc. MicroNanotechnology for Space Application (April 1999)* vol 1

[7] Rossi C *et al* 1999 A new generation of MEMS based microthrusters for microspacecraft applications *Proc. MicroNanotechnology for Space Applications (April 1999)* vol 1

[8] Musser G and Alpert M 2000 How to go to Mars *Sci. Am.* **282** 44–51

[9] Koeneman P B, Busch-Vishniac I J and Wood K L 1997 Feasibility of micro power supplies for MEMS *J. Microelectromech. Syst.* **6**

[10] Purrington G W 1989 Plastic resin bonded high energy rocket fuel systems *Firefox Enterprises Inc.*

[11] Kishore K and Gayarthri V 1984 Chemistry of ignition and combustion of ammonium-perchlorate-based propellants *Fundamentals of Solid Propellant Combustion Prog. in Astronautics and Aeronautics* vol 90, ed K K Kuo and M Summerfield ch 2

[12] Sigman R K, Price E W, Chakravarthy S R and Zachary E K 1996 Subignition heating tests for flake and powdered aluminum *Proc. 3rd Annu. JANNAF Combustion Meeting (Monterey, CA, CPIA Nov. 1996)*

[13] Ayon A, Bayt R, Lin C, Braff R, Sawin H and Schmidt M 1998 Etching characteristics and profile control in a time multiplexed inductively coupled plasma etcher *Sensors and Actuators Workshop (Hilton Head 1998)*

[14] Janson S and Helavijian H 1996 Batch-fabricated microthrusters: initial results 32nd *SISS/ASME/SAE/ASEE Joint Propulsion Conf. (Lake Buena Vista, FL, 1996)*

[15] Bayt R L, Breuer K S and Ayon A A 1998 DRIE-fabricated nozzles for generating supersonic flows in micropropulsion systems *Proc. Solid-State Sensor and Actuator Workshop (Hilton Head, S C, June 1998)*

[16] Williams F A 1985 *Combustion Theory* 2nd edn (Menlo Park, CA: Benjamin-Cummings)

[17] Baltes H, Moser D and Freidemann V 1994 Thermoelectric microsensors and microsystems mechanical sensors *Sensors* vol 7, ed H H Bau, B de Rooji and Kloeck (Weinheim: VCH) pp 13–55

[18] Jaeggi D 1996 Thermal converters by CMOS technology *PhD Thesis* (Zurich: Physical Electronics Laboratory)

[19] Leggenhager R and Baltes H 1993 Improved thermoelectric infrared sensor using double poly CMOS technology *Int. Conf. on Solid-State Sensors and Actuators (Transducers '93) (June 1993)* pp 1008–11

[20] Muller M *et al* 1995 A thermoelectric infrared radiation sensor with monolithically integrated amplifier stage and temperature sensor *Int. Conf. on Solid-State Sensors and Actuators (Transducers '95) (June 1995)* pp 640–3

[21] Olgun Z, Akar O, Kulah H and Tayfun 1997 An integrated thermopile structure with high responsivity using any standard CMOS process *Int. Conf. on Solid-State Sensors and Actuators (Transducers '97) (June 1997)* pp 1263–6